

Composite acousto-optical modulation

Ruijuan Liu, Yudi Ma, Lingjing Ji, Liyang Qiu, Minbiao Ji, Zhensheng Tao, Sajun Wu
Department of Physics, State Key Laboratory of Surface Physics and Key Laboratory of Micro and Nano Photonic Structures (Ministry of Education), Fudan University, Shanghai 200433, China.

(Dated: March 11, 2022)

We identify a new class of acousto-optical modulation (AOM) schemes based on composite diffraction by multiple AOMs. We show that by adjusting the amplitudes and phases of weakly-driven daughter AOMs re-imaged by 4-F optics, the composite AOM can be optimized for highly efficient optical diffraction beyond the Bragg condition. Furthermore, by re-imaging counter-propagating sound waves, rapid switching of output orders can be achieved at the driving radio frequency (rf) limit toward GHz level. Here, a proof-of-principle demonstration with a simplest example using two AOMs demonstrates a uniform $> 90\%$ diffraction efficiency over a wide rf-tuning bandwidth, with which we route a mode-locked laser pulse train into two paths with $15 \sim 20$ dB side-pulse suppression. With the unprecedented acoustic optical modulation efficiency and bandwidth combination, we expect the composite technique to help paving a practical pathway toward arbitrary modulation of mode-locked lasers for applications across fields.

I. INTRODUCTION

The developments of ultrafast technologies [1–4] have dramatically enhanced our ability to access physics at various time scales with finest precision. To utilize the pulsed lasers for nonlinear optical control [5–7] and spectroscopic measurements [8, 9], pulse shaping techniques have been developed in the frequency and time domain to produce optical waveforms with optimally tailored spectra-phases [10, 11]. To flexibly control and individually shape the output pulses, one would like to modulate each pulse j in terms of amplitude, phase, and propagation direction. The simplest example of such pulse modulation is to pick up pulse j into direction \mathbf{k}_{out} only when the pulse number j is an integer multiple of M , so as to prescale the repetition rate of the mode-locked laser output from f_{rep} to $f'_{\text{rep}} = f_{\text{rep}}/M$. The standard method to implement the pulse picking is through electro-optical modulation (EOM) with Pockels cells. However, the Pockels cells can hardly operate beyond a 10 MHz rate since it is difficult to generate the powerful high-voltage waveforms while managing the dissipation [12]. Unlike high-voltage requirements for EOM, low-voltage rf signals can transduce crystal sound waves in acousto-optical modulators (AOM) to control the optical output with accurately programmable Bragg diffraction [13–15]. In addition to enabling arbitrary pulse picking with unlimited duty cycle [16], an excellent example to illustrate AOM pulse modulation is to shift the phase of individual pulses so as to stabilize the carrier-envelop phase of a frequency comb [17–19]. However, since efficient AOM diffraction relies on phase-matching the light beams with the sound wave, in traditional AOM schemes the tuning range and control bandwidth for diffracting multi-color light are severely limited. For example, the moderate AOM control bandwidth is hardly wide enough for efficient modulation of mode-locked lasers, when the repetition rate is at ~ 100 MHz level or higher.

As is well known, the dynamics of para-axial light propagation in AOM is mathematically equivalent to

those of matterwave in a pulsed standingwave potential. It is therefore possible to borrow standard techniques from one field of applications to the other. Inspired by coherent control techniques for atom interferometry [20–22], we propose a new class of techniques to operate AOMs beyond the Bragg condition and for rapid modulation with close-to-unity diffraction efficiency. The key idea is summarized in Fig. 1. By optically linking a series of AOMs with 4-F imaging systems (Fig. 1b), the Bragg-diffraction by a single AOM is coherently split into a N -AOM process. The $2N - 1$ amplitude and relative phase degrees of freedom, $\{A_j, \varphi_j\}$, can be continuously adjusted to optimize for specific light control applications. In particular, when each “daughter” AOM is only weakly driven, a 2-mode approximation maps the composite diffraction dynamics to time-domain spin control, where composite pulse techniques are developed to universally enhance the resilience to control errors [23–25]. Key performance parameters such as the diffraction efficiency can then be optimized for *e.g.*, efficient diffraction of multi-color beams over a broad range of sound wave frequency even when the Bragg condition is severely violated. Furthermore, when counter-propagating sound waves are re-imaged together (Fig. 2), interference of diffraction amplitudes leads to rapid switching of the output at twice the rf driving frequency ω_S , which can be exploited for efficiently routing a pulse train with up to GHz repetition rate into multiple directions. We expect the composite technique to enable advanced AOM applications with both CW [14, 15, 26] and pulsed lasers [16–18, 27, 28]. We notice related schemes of composite-pulse-inspired error-resilient 2-mode optical control have been derived [29–31] in scenarios where a mode-truncation as in this work is not required.

The remainder of this paper is structured as following. First, in Sec. 2, we derive the input-output relation for the 4-F re-imaged weakly driven AOM system (Fig. 1), compare it with the well-established SU(2) coherent control formalism [24, 25], and point out the opportunity of constructing composite AOM with pro-

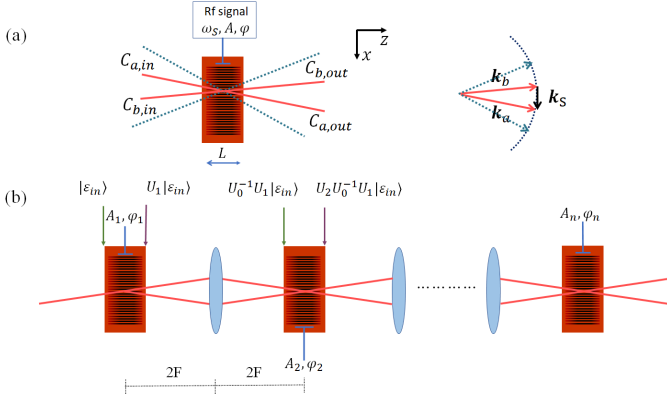


FIG. 1. Operational principle of the composite AOM scheme. Light beams with wavevector $\mathbf{k}_{a,b}$ and wavefronts $C_{a,b}$ are Bragg-coupled by the sound wave with wavevector \mathbf{k}_S . The approximate phase-matching $\mathbf{k}_a - \mathbf{k}_b \approx \mathbf{k}_S$ is illustrated in (a) on the right. When the AOM is weakly driven, the diffraction orders off the Bragg condition (represented by dashed lines) can be ignored. The input-output relation for the optical wavefront can then be represented by $|\mathcal{E}_{\text{out}}\rangle = U|\mathcal{E}_{\text{in}}\rangle$, with evolution operator $U(t, re^{i\varphi}) = (t, re^{i\varphi}; -r^* e^{-i\varphi}, t^*)$ controlled by the rf signal to transform a (C_a, C_b) spinor. This input-output relation are applied iteratively in (b) for multiple re-imaged nearly identical AOMs with $U_j = U(t_j, r_j e^{i\varphi_j})$. With the output wavefront of each AOM, $|\mathcal{E}_{j,\text{out}}\rangle$ imaged to the exit window of the next AOM, the wavefront at the entrance window of the next AOM is give by $|\mathcal{E}_{j+1,\text{in}}\rangle = U_0^{-1}|\mathcal{E}_{j,\text{out}}\rangle$, with U_0^{-1} effectively evolving the wavefront backward over the interaction length L in absence of acousto-optical diffraction.

grammable spatial-temporal features unattainable with single AOMs. In Sec. 3 we specifically discuss a simple example of the composite scheme in close analogue to a double-diffraction scheme in atom interferometry [20, 21], and present the experimental demonstration of this double-AOM scheme where a composite diffraction efficiency of $\bar{R}_{\text{max}} > 90\%$ is uniformly achieved when the driving rf frequency deviates from the Bragg-resonant value by $\sim \pm 30\%$. We further demonstrate rapid routing of a $f_{\text{rep}} = 80$ MHz mode-locked laser output into two paths with close-to-unity efficiency and $15 \sim 20$ dB side pulse suppression. In Sec. 4 we discuss extension of the double-AOM scheme for high speed, high contrast repetition rate prescaling at GHz level, and take an outlook to possible applications of the composite AOM schemes.

II. COMPOSITE AOM BY 4-F IMAGING - THEORY

We consider composite AOM setup schematically illustrated in Fig. 1b where light diffracted by one AOM is re-imaged to another via a 4-F imaging system. For each single AOM operation (Fig. 1a), the para-axial propagation of light in the index field $n(\mathbf{r}, t)$ along \mathbf{e}_z , with $E = \mathcal{E}e^{i\bar{n}k_0z}$ obeying $(\nabla^2 + n^2 k_0^2)E = 0$, is characterized

by a slowly varying amplitude \mathcal{E} with

$$i\partial_z \mathcal{E} = -\frac{1}{2\bar{n}k_0} \nabla_{\perp}^2 \mathcal{E} - \delta n k_0 \mathcal{E}. \quad (1)$$

Here \bar{n} is the refractive index of the AOM crystal, for example, $\bar{n} \approx 2.3$ for TeO_2 at near infrared. An rf-driven traveling sound wave with a strain amplitude η leads to a rapidly varying refractive index deviation $\delta n = n - \bar{n}$ as

$$\delta n = \eta \frac{1 - \bar{n}^2}{2\bar{n}} \cos(k_S x - \omega_S t + \varphi). \quad (2)$$

The slowly varying envelops of the density wave are described by the phase $\varphi(\mathbf{r} - \mathbf{v}_S t)$ and amplitude $\eta(\mathbf{r} - \mathbf{v}_S t)$ functions, which are controlled by those of the driving rf-fields through rf-to-sound transducers, and propagate with the group velocity \mathbf{v}_S along \mathbf{e}_x , with $v_S = \omega_S/k_S$ for the linearly dispersive crystal. For example, in TeO_2 the longitudinal sound velocity is $v_S = 4260$ m/s. The detailed spatial dependence is determined by the crystal geometry and the location of the transducers. Here, without losing generality we simply assume a stationary and spatially uniform φ , and a stationary amplitude following a step-wise distribution as constant η for $0 < z < L$ and zero otherwise.

The equivalence between Eq (1) and the two-dimensional Schrödinger equation allows us to introduce Dirac notation $|\mathcal{E}(z)\rangle$, with $\mathcal{E}(\mathbf{r}_{\perp}, z) = \langle \mathbf{r}_{\perp} | \mathcal{E}(z) \rangle$, to conveniently describe the wavefront of the optical mode-function propagating along z . The input-output relation for the wavefront through the $0 < z < L$ interaction can then be generally expressed as $|\mathcal{E}_{\text{out}}\rangle = U|\mathcal{E}_{\text{in}}\rangle$ by an evolution operator $U = e^{-iHL}$ that integrates the interaction by the Hamiltonian

$$H = -\frac{1}{2\bar{n}k_0} \nabla_{\perp}^2 + \eta \frac{\bar{n}^2 - 1}{2\bar{n}} k_0 \cos(k_S x + \varphi). \quad (3)$$

Notice this H governs the paraaxial wavefront propagation along z , with t merely as a parameter. We have thus absorbed the $-\omega_S t$ term in Eq. (2) into $\varphi(t)$ for conciseness in the following. Equation (4) can be re-written in the k -space as $H = H_0 + \int d^2 \mathbf{k}_{\perp} V(\mathbf{k}_{\perp})$, with $H_0 = \frac{1}{2\bar{n}k_0} \mathbf{k}_{\perp}^2$ and

$$V(\mathbf{k}_{\perp}) = \frac{K}{2} e^{i\varphi} |\mathbf{k}_{\perp} + \mathbf{k}_S \rangle \langle \mathbf{k}_{\perp}| + \text{h.c.} \quad (4)$$

Physically, V couples an “infinite” set of wavefronts shifted in \mathbf{k}_{\perp} -space by multiple $\mathbf{k}_S = k_S \mathbf{e}_x$. The coupling constant $K = \eta k_0 (\bar{n}^2 - 1)/2\bar{n}$ can be referred to as a “spatial Rabi frequency” [21]. We restrict ourselves to input wavefronts near a lowest order Bragg-resonance, $\langle \mathbf{r}_{\perp} | \mathcal{E}(z=0) \rangle = C_a(\mathbf{r}_{\perp}, 0) e^{-ik_S x/2} + C_b(\mathbf{r}_{\perp}, 0) e^{ik_S x/2}$ with $C_{a,b}$ confined to $|k_x| < k_S/2$ in the k -space. Consider a diffraction “pulse area” $\Theta = KL$, a weak drive condition of

$$\Theta \ll \frac{k_S^2}{\bar{n}k_0} L \quad (5)$$

allow us to truncate the wave propagation by Eq. (1) in k to obtain $\langle \mathbf{r}_\perp | \mathcal{E}(z) \rangle \approx C_a(\mathbf{r}_\perp, z) e^{-ik_{\text{S}}x/2} + C_b(\mathbf{r}_\perp, z) e^{ik_{\text{S}}x/2}$. The pair of Bragg-coupled wavefronts obey

$$\begin{aligned} i\partial_z C_a &= \frac{(\mathbf{k}_\perp - \mathbf{k}_{\text{S}}/2)^2}{2\bar{n}k_0} C_a + \frac{\Theta}{2L} e^{-i\varphi} C_b, \\ i\partial_z C_b &= \frac{(\mathbf{k}_\perp + \mathbf{k}_{\text{S}}/2)^2}{2\bar{n}k_0} C_b + \frac{\Theta}{2L} e^{i\varphi} C_a. \end{aligned} \quad (6)$$

in the k -space, *i.e.* with $C_{a,b}(\mathbf{k}_\perp, z)$ to be the 2D Fourier transform of $C_{a,b}(\mathbf{r}_\perp, z)$. By parametrizing $(C_a, C_b) = (\cos(\frac{\theta}{2})e^{-i\phi/2}, \sin(\frac{\theta}{2})e^{i\phi/2})$ and introducing a wavevector mismatch $\delta k = k_x k_{\text{S}}/\bar{n}k_0$, the dynamics of the spinor is mapped to that for a unit vector $\mathbf{r} = (\sin\theta \cos\phi, \sin\theta \sin\phi, \cos\theta)$ on a Bloch sphere (Fig. 2b):

$$\frac{d}{dz} \mathbf{r} = \mathbf{K} \times \mathbf{r}. \quad (7)$$

Here $\mathbf{K} = (K \cos\varphi, K \sin\varphi, \delta k)$ is a “spatial Rabi vector”. Clearly, for incident beam with $\mathbf{k}_\perp = \{k_x, k_y\}$, $|k_x| \ll \frac{\bar{n}k_0}{k_{\text{S}}L}$ is required to support a \mathbf{k}_\perp -insensitive Θ -operation near the Bragg condition. One might try to improve the broadband performance simply by reducing the interaction length L . However, for a fixed Θ -operation such as to Bragg-deflect the incident beam with $\Theta = \pi$, a reduced L typically leads to increased AOM strength $K = \Theta/L$ to compromise the weak drive condition by Eq. (5), resulting in high-order diffraction losses. Indeed, commercially available AOMs are usually optimized near $\Theta = \pi$ with an interaction length L that balances the broadband operation with the weak drive condition. The compromise is partially responsible for the never perfect Bragg-diffraction using commercially available AOMs.

So far, we merely reformulate standard AOM Bragg-diffraction theory with notations of quantum mechanics. Nevertheless, they allow us to confirm the validity of the 2-mode approximation and to apply composite control theory [21, 24, 25] for the $C_{a,b}$ control next. In particular, we consider the setup in Fig. 1b where multiple AOMs are re-imaged by the 4-F optics. Within the 2-mode approximation, each “daughter-AOM” j transforms $\{C_a, C_b\}$ with a unitary matrix $U(t_j, re^{i\varphi_j}) = (t_j, r_j e^{i\varphi_j}; -r_j^* e^{-i\varphi_j}, t_j^*)$, which can be obtained by integrating Eq. (6) and being visualized on the Bloch sphere (Fig. 2b). Furthermore, since the 4-F system images the output at $z = L$ to the entrance of the next AOM locally at $z' = 0$, the wavefront effectively evolves backward along z with $U_0^{-1} = e^{iH_0L}$, which can also be obtained from Eq. (6) with $\Theta = 0$ and visualized on the Bloch sphere as precession of \mathbf{r} around $\mathbf{K}_0 = (0, 0, -\delta k)$. More generally, the transformation of the wavefront by the composite AOM is described as $|\mathcal{E}_{\text{out}}\rangle = \bar{U}|\mathcal{E}_{\text{in}}\rangle$, with (with $\prod_{j=1}^n$ for multiplying from left)

$$\bar{U} = U_0 \prod_{j=1}^n (U_0^{-1} U_j). \quad (8)$$

One should thus be able to adjust $\{A_j, \varphi_j\}$ of each daughter AOM to optimize \bar{U} and the output wavefront $|\mathcal{E}_{\text{out}}\rangle$.

Specifically, within the 2-mode approximation, the matrix $\bar{U} = (\bar{t}, \bar{r}; -\bar{r}^*, \bar{t}^*)$ is constructed in essentially the same way as those for achieving 2-level robust population inversion [21, 24] and universal qubit gates [25]. The wavevector mismatch δk and diffraction pulse area Θ_j are in direct analogy to the detuning and the pulse area in 2-level spin-controls [24, 25]. The associated formula can thus be applied here to improve the robustness of beam-splitting [25] or deflection [21, 24] against deviation of these AOM operation parameters, which may arise during *e.g.* broadband diffraction of ultrafast pulses [17–19]. In addition, high-order diffraction leakage which generally limits the efficiency of single AOMs may be dynamically suppressed in the composite scheme, similar to those in multi-level quantum control [23].

III. A DOUBLE-AOM SCHEME

We leave an experimental investigation of the N-AOM diffraction scheme (Fig. 1b) with $N \geq 3$ for a future work. In the following we take the simplest example of a double-AOM scheme to demonstrate the powerfulness of the composite diffraction for broadband, flexible control of a mode-locked laser.

A. Operation principles

With Eqs. (6)(7)(8), it is straightforward to understand the operation principle of the double-AOM scheme in Fig. 2 which is implemented in this work to route a mode-locked laser pulse train into two directions. As illustrated in Fig. 2a, practically the 4-F optics to re-image the wavefronts through $\text{AOM}_{1,2}$ are composed of $l_{1,2}$ in the standard 4-F configuration to ensure the imaging precision. The re-imaged sound waves in $\text{AOM}_{1,2}$ can be chosen to co-propagate or to counter-propagate. As by Eqs. (2)(4), a flip of \mathbf{k}_{S} sign effectively change the time-dependence of the sound-wave phase $\varphi_j(t) = \varphi_j(0) \pm \omega_{\text{st}}$.

To understand the dynamics of double-AOM, it suffices to analyze the composite \bar{U} by Eq. (8) at a specific time t for $\text{AOM}_{1,2}$ with a specific driven amplitude $A_{1,2}$ and phase $\varphi_{1,2}$. According to Eq. (7), to achieve an optimal diffraction $\bar{R} \equiv |\bar{r}|^2$ (Fig. 2(b,i)), the coherent control strategy should be that AOM_1 rotate the state vector \mathbf{r} to the equator of the Bloch sphere with \mathbf{K}_1 , which, after a free precession by \mathbf{K}_0 , be rotated again by \mathbf{K}_2 with optimal $\Delta\varphi_{2,1} = \varphi_2 - \varphi_1$ to complete the spin inversion. Optimal diffraction with $\bar{R} \approx 1$ could thus be obtained even at large wavevector mismatch $\delta k \leq \pi/\sqrt{2L}$, by properly adjusting $\{A_{1,2}, \varphi_{1,2}\}$ of $\text{AOM}_{1,2}$. The strategy is in direct analogy to the double-diffraction method in atom interferometry [20, 21]. We note that the optical phase of the deflected beam follows $\bar{\varphi}_{1,2} = (\varphi_1 + \varphi_2)/2$ for flexible optical phase control [14, 17]. On the other hand, to minimize \bar{R} so as to recover $\bar{T} \equiv |\bar{t}|^2$ to unity

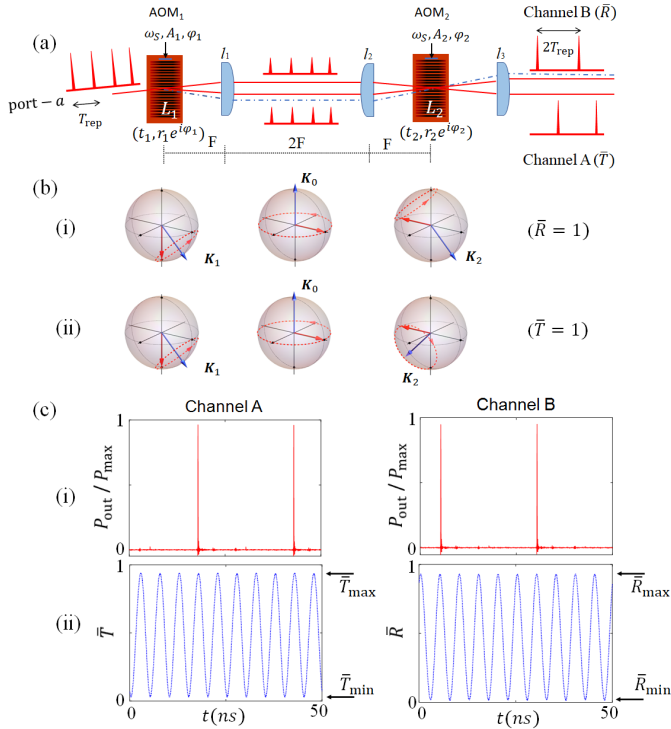


FIG. 2. The double-AOM scheme for efficiently routing a mode-locked pulse train with AOM diffraction beyond the Bragg condition. In (a), AOM_{1,2} with $L_1 \approx L_2$ are imaged by a 4-F system with counter-propagating sound waves. A pulse train from a picosecond oscillator with $T_{\text{rep}} = 1/f_{\text{rep}}$ is subsequently diffracted by AOM_{1,2}. When the sound-wave frequency is set as $\omega_S = \pi f_{\text{rep}}(2\nu + 1)/2$ with ν as an integer, $\Delta\varphi_{1,2}(t) = 2\omega_S t + \Delta\varphi_{1,2}(0)$ is incremented by π for any pulse pair separated by T_{rep} . By adjusting $\Delta\varphi_{1,2}(0)$ and AOM driving amplitudes $A_{1,2}$, full switching from $\bar{R} = 1$ to $\bar{T} = 1$ can be achieved. The effective diffraction mechanisms under the 2-mode approximation are illustrated in (b,i) and (b,ii) on a Bloch sphere, for the case of a large wavevector mismatch $\delta k \approx \pi/L\sqrt{2}$ (corresponding to the diffraction path marked with dashed blue line in (b)). Typical experimental measurements for routing a $f_{\text{rep}} = 80$ MHz picosecond pulses are given on (c,i) leading to 30:1 and 100:1 side-pulse suppression. The time-dependent diffraction \bar{R} and transmission \bar{T} measured by a CW laser are given in (c,ii), with $\{(\bar{T})_{\text{max}}, (\bar{R})_{\text{max}}\} = \{0.94, 0.93\}$, $\{(\bar{T})_{\text{min}}, (\bar{R})_{\text{min}}\} = \{0.04, 0.02\}$. The slightly decreased contrast in the CW case is likely related to the finite response time of the photon detector.

(Fig. 2(b,ii)), an additional π should be added to $\Delta\varphi_{2,1}$ so that AOM₂ undoes the rotation of \mathbf{r} by AOM₁.

We now discuss the time-dependence of the double-AOM in the Fig. 2a setup. The counter-propagating sound-wave re-imaged by the 4-F system as in this work leads to rapidly scanning $\Delta\varphi_{1,2}(t) = 2\omega_S t + \Delta\varphi_{1,2}(0)$ at twice the rf frequency. For the optimally adjusted $\{A_1, A_2\}$ as discussed above, an $\omega_S = (2\nu + 1)\pi f_{\text{rep}}/2$ with integer ν should result in a π phase increment in $\Delta\varphi_{1,2}$ for two successive pulses separated by $T_{\text{rep}} = 1/f_{\text{rep}}$. By properly pre-adjusting $\varphi_{1,2}(0)$, rapid switch-

ing of the composite AOM output between $\bar{R} = 1$ and $\bar{T} = 1$ can be achieved (Fig. 2c) to route the adjacent pulses from a mode-locked laser into two directions.

B. Experimental implementation

We demonstrate the double-AOM scheme for efficiently modulating both CW and pulsed lasers. As being summarized by Fig. 2a, a pair of AOMs (AA optoelectronic, MT-110-A1) are aligned to operate at $\omega_S = 2\pi \times 100$ MHz to Bragg-deflect the laser beam from a single-mode optical fiber into port-*a*. Phase-stable rf signals from a programmable multi-channel synthesizer (NovaTech 409B) are amplified to drive the sound waves. AOM₂ is re-imagined to AOM₁ by a pair of achromatic lenses $l_{1,2}$ with $F = 100$ mm focal length. The waist radius $w \approx 110 \mu\text{m}$ for the incident Gaussian beams are large enough to support $|r_{1,2}|^2 \approx 80\%$ with each of the two AOMs (Fig. 4(a)). To achieve composite AOM, the relative alignment starts with switching on a single AOM_j only, with A_j adjusted to achieve $|r_j|^2 \approx 0.5$ half deflection. Nearly identical beam splitting by AOM_{1,2} into the output Channels *A* and *B*, with nearly identical output shapes in each case, are confirmed by recording the outputs with a digital camera. Next, fine alignments are achieved by switching on both AOM_{1,2} with reduced $|r_{1,2}|^2 \sim 0.3$ and by injecting the single-mode fiber with a synchronized pulse train with $\tau = 0.5$ ns pulse duration [32] at $f_{\text{rep}} = 100$ MHz. By shifting the $l_{1,2}$ location and finely orienting AOM₂, the AOM_{1,2} diffractions are mode-matched, leading to uniformly varying output beams on the camera when $\Delta\varphi_{1,2}(0)$ is slowly scanned. Further improvements to the alignment is achieved by optimizing the contrast of the time-dependent transmission \bar{T} (from Channel *A*) and diffraction \bar{R} (from Channel *B*) at 200 MHz with a CW laser, using a multi-mode-fiber coupled fast photodetector (Thorlabs DXM12DF), see Fig. 2c for example. Finally, the rf amplitudes $A_{1,2}$ are scanned to finely locate $|r_{1,2}|_{\text{opt}}^2 \approx 0.5$ that maximize the composite diffraction efficiency \bar{R}_{max} . Typical $|r_{1,2}|^2$ -scan 2D data for the CW laser modulation are shown in Fig. 3a. The optimal $|r_{1,2}|_{\text{opt}}^2$ values at $\omega_S = 2\pi \times 100$ MHz are marked with white dashed lines.

To operate the double-AOM as a bi-directional pulse router, a picosecond mode-locked laser (Spectra-Physics Tsunami system) with $f_{\text{rep}} = 80$ MHz is injected to port-*a* through the same single mode fiber in this work. The Novatech rf source is synchronized with the laser pulses, by phase-locking the Novatech clock with a 10 MHz laser synchronization signal. A $\delta\tau \approx 100$ ps relative jitter between the laser pulses and the rf signal is found to be primarily limited by the phase locking quality in this simple synchronization scheme. By adjusting $\Delta\varphi_{1,2}(0)$, adjacent pulses with $T_{\text{rep}} = 12.5$ ns inter-pulse spacing are alternating routed into Channel *A* and *B*, as demonstrated in Fig. (2c). Excluding the $\sim 5\%$ overall insertion loss, the efficiency for pulse picking in Channel *A*(*B*) reaches 96%

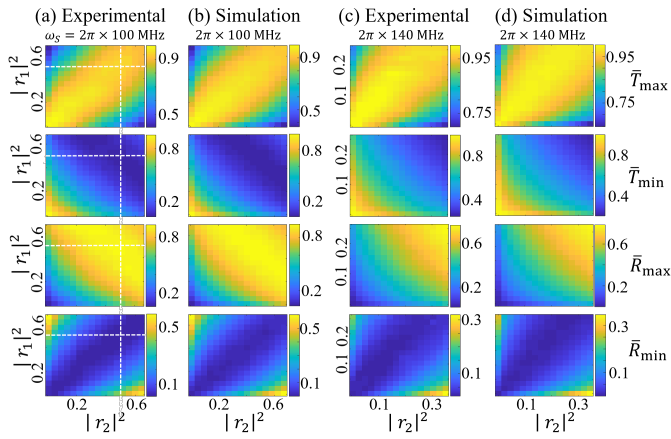


FIG. 3. Fine tuning of $|r_{1,2}|^2$ to optimize \bar{R}_{\max} for the double-AOM scheme. The experimentally measured $\bar{T}_{\max, \min}$ and $\bar{R}_{\max, \min}$ are given in column (a,c) (with raw data re-interpolated to evenly spaced $|r_{1,2}|^2$ grids) to be compared with the simulated data in column (b,d) based on the Eq. (1) model with $L = 8$ mm. The AOMs as by Fig. 2a are optimally aligned at $\omega_S = 2\pi \times 100$ MHz, with corresponding data displayed in column (a,b). Data for $\omega_S = 2\pi \times 140$ MHz operation which substantially violates the Bragg condition are shown in column (c,d).

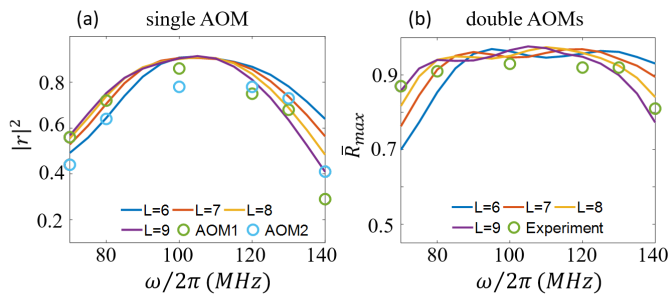


FIG. 4. Optimal deflection efficiency measured for single AOM (a) and double AOMs (b). Simulated data based on the Eq. (1) model parametrized by various interaction length L (mm) are displayed for comparison.

(94%), with a contrast reaching 30:1 (100:1) respectively relative to the suppressed side pulses. Notice this contrast is compromised slightly by the time jitter $\delta\tau$, which should be improvable to 1 ps level via *e.g.*, direct digital synthesizing of the rf signals.

We now demonstrate efficient double-AOM deflection when the Bragg condition is substantially violated by a large δk mismatch. For the purpose, we shift the sound-wave frequency ω_S away from 100 MHz and measure the maximum diffraction efficiency \bar{R}_{\max} optimized with $\{A_j, \varphi_j\}$, at sound wave frequency as large as $\omega_S = 2\pi \times 140$ MHz. The electronic optimization process to obtain \bar{R}_{\max} in Fig. 3c is identical to those for achieving $|r_{1,2}|_{\text{opt}}^2$ in Fig. 3a for the case of $\omega_S = 2\pi \times 100$ MHz, by

retrieving $\{\bar{R}_{\min}, \bar{R}_{\max}\}, \{\bar{T}_{\max}, \bar{T}_{\min}\}$ from Channel A/B with CW laser measurements (Fig. 2(c,ii)). With the Bragg condition aligned at $\omega_S = 2\pi \times 100$ MHz, a 40% deviation of ω_S leads to $k_x = 0.4k_S$ and $\delta k = 0.4k_S^2/\bar{n}k_0 \approx \pi/(\sqrt{2} \times 10$ mm). According to the analysis in Sec 3.1, if the sound field interaction length L is within 10 mm, then the 2-mode theory predicts a maximum $|r_{1,2}|^2 \geq 0.5$ and nearly perfect $\bar{R}_{\max} \approx 1$. Practically, we find $|r_{1,2}|^2$ saturate to 0.3 and 0.4 respectively (Fig. 4a), likely due to a lack of rf power in our setup to fully drive the sound wave in presence of significant impedance mismatch. Nevertheless, guided by the effective theory we are able to locate $\bar{R}_{\max} = 0.82$ at optimal $|r_{1,2}|^2$ and $\Delta\varphi_{1,2}$, as in Fig. 3c and Fig. 4b. We further measure \bar{R}_{\max} for ω_S between 70 MHz and 140 MHz, with $\bar{R}_{\max} > 90\%$ uniformly achieved between 80 and 130 MHz (Fig. 4b).

Finally, instead of routing the $f_{\text{rep}} = 80$ MHz picosecond laser into two paths, the broadband deflection supported by the double-AOM system allows us to synchronize the composite diffraction with the mode-locked laser at $\omega_S = 2\pi \times 80$ MHz, without realigning the optics, to directly observe the channel A/B output intensity profiles with a slow camera. Figure 5 gives such measurements when $\Delta\varphi_{1,2}(0)$ is adjusted to give $\bar{R} \approx 0.5, 0$ and 1 respectively. As in Figs. 5b,5c, for the case of $\bar{R} \approx 0, 1$, the residual output in the A/B ports are so weak, that we have to over-expose the camera to see the residual features. These residual features provide us with clue on what is limiting the pulse routing efficiency and contrast for future improvements of the double-AOM system.

We find $\Delta\varphi_{1,2}$ stays optimal in our temperature stabilized lab for tens of hours at least without noticeable drifts. The excellent passive phase-stability is due to common-mode rejection of drifting and vibrational noises by the two diffraction orders (Fig. 2a), which share all the optics during their propagation and are within one millimeter to each other spatially. A more precise quantification of the short and long-term phase-stability will be for a future work.

To further understand the double-AOM system beyond the 2-mode approximation, we numerically integrate the 1D AOM model outlined in Sec. 2 according to the original Eq. (1). As discussed there, in the simple model the sound fields have a “step-function” distribution with an interaction length L . We simulate the performance of single and double-AOM with the model with various L to match the experiments. By comparing the simulations with the experimental measurements, as in Fig. 4, an effective $L = 7 \sim 8$ mm interaction length can be inferred with which we further simulate the $|r_{1,2}|^2$ -tuning process as those in Fig. 3(b,d), with very good global agreements. It should be noted that the actual sound field distribution is more complicated and may vary among AOMs. We expect even better performance once these details are included in the modeling, followed by fine imaging and tuning of specific two-AOM systems.

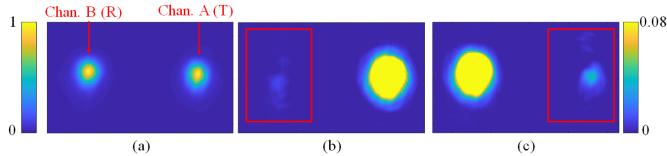


FIG. 5. The output of the composite AOM recorded by a digital camera. The alignment of the double-AOM is optimized at $\omega_S = 2\pi \times 100$ MHz to route a $f_{\text{rep}} = 80$ MHz picosecond laser alternating into Channel A/B respectively. Here we instead set $\omega_S = 2\pi \times 80$ MHz to synchronize with f_{rep} . By adjusting $\Delta\varphi_{1,2}(0)$, $\bar{R} \approx 0.5, 0, 1$ are achieved for all the pulses for the slow camera recording, as being displayed in (a),(b),(c) respectively. The re-scaled colorbar on the right is for Figs. (b, c) to highlight the weak residuals in the A/B channels.

IV. DISCUSSIONS

Acousto-optical modulators are ubiquitously equipped in modern research labs across fields for modulation of amplitude, phase, frequency and propagation direction of light. Efficient AOM diffraction relies on phase-matching the light beams with the sound wave. Deviation of operation parameters from the pre-aligned Bragg condition leads to reduced diffraction efficiency and distorted diffraction phase. Therefore, in traditional AOM applications, the tuning range and control bandwidth for multi-color light are severely limited. The limitation in the AOM control bandwidth represents a more general gap in laser modulation technology today, as being pointed out in ref. [33], at the nanosecond time scale.

In this work, we have proposed a novel approach to control light with acousto-optical modulation by coherently splitting a single AOM diffraction into an N-AOM process. We have shown that the diffraction dynamics of the weakly driven N-AOM system can be mapped to time-domain spin control where composite techniques are developed to universally enhance the resilience to control errors [23–25]. Toward the 2-mode approximation for highly efficient diffraction, the weakly driving condition (Eq. 5) is more easily met by the composite scheme. Conversely, the fact that composite AOM only needs to be weakly driven makes AOM based on crystalline quartz, which are typically more difficult to deeply drive but are more amenable to ultrafast control with low insertion losses [34], a favorable choice for constructing the N-AOM system. Finally, we note that the discussions in this work have been restricted to isotropic acousto-optical interactions. With proper modification of the simple theory, the composite diffraction technique may also be applied to acousto-optical devices based on birefringent response of slow shear waves [26, 35].

Experimentally, with a simplest example in analogue to the “double-pulse” technique [20–22], we have demonstrated that a two-AOM system can efficiently route a synchronized pulse train into two directions, and can

maintain a high diffraction efficiency even when the Bragg condition is severely violated. Similar to the single-AOM case, for the double-AOM scheme in this work the optimal $\bar{R} \approx 94\%$ diffraction efficiency is still limited by high-order diffraction losses and to a less degree by the δk -mismatch for the $w = 110 \mu\text{m}$ beam. Numerical simulations suggest $\bar{R} \sim 99\%$ level is achievable by better mode-matching the double-AOM diffraction and then by moderately increasing L and w together. The requirements are expected to relax in N-AOM system with $N \geq 3$, which should be explored in future work for broadband, achromatic control of laser beams.

For the application of the double-AOM system, we notice the rapid switching between $\bar{R} = 1$ and $\bar{T} = 1$ as in Fig. 2 is a result of diffraction interference and does not requiring tightly focusing the laser beam under control. The pulse router function can thus be applied to laser pulses with much higher power than those by traditional pulse pickers, when subjecting to a same level of AOM optical intensity damage threshold. The moderate $15 \sim 20$ dB contrast of the side-pulse suppression can be improved by increasing L and w , as being discussed above. A more straightforward way to improve the contrast to $30 \sim 40$ dB level is to apply the double-AOM system again to a selected output channel, at a small cost of overall efficiency. Operating at the driving rf frequency limit, the double-AOM method enable efficient bi-directional pulse routing at very high repetition rate, with $f_{\text{rep}} = 400$ MHz already in this work and easily extendable to a GHz rate. The high pulse picking efficiency should in addition support one to iteratively apply the double-AOM system for multi-directional pulse routing at the GHz rate. The exceptionally broad rf-tuning range may help the composite AOM scheme to stabilize the carrier-envelop phase [17–19] of a few-cycle femtosecond pulse, in combination with the efficient and stable pulse compression technique recently developed [36]. Our method may also extend the modulation schemes and pulse shaping techniques used for coherent Raman imaging, enabling fast frequency, amplitude and polarization modulations, to achieve spectral multiplexing and background suppression [37–39].

FUNDING INFORMATION

National Key Research Program of China (2017YFA0304204); National Natural Science Foundation of China (12074083,61975033,1874121); The Shanghai Municipal Science and Technology Basic Research Project (19JC1410900).

ACKNOWLEDGEMENTS

We thank Ruochen Gao, Yuxiang Zhao, Jiangyong Hu and Xing Huang for experimental assistance and discussions. We thank Prof. Yanting Zhao and Prof. Lin

Zhou for helpful discussions during the development of this project.

DISCLOSURES

The authors declare no conflicts of interest.

DATA AVAILABILITY

Data underlying the results presented in this paper are not publicly available at this time but may be obtained from the authors upon reasonable request.

[1] H. A. Haus, Mode-locking of lasers, *IEEE Journal on Selected Topics in Quantum Electronics* **6**, 1173 (2000).

[2] S. T. Cundiff and J. Ye, Colloquium: Femtosecond optical frequency combs, *Reviews of Modern Physics* **75**, 325 (2003).

[3] F. Krausz and M. Ivanov, Attosecond physics, *Reviews of Modern Physics* **81**, 163 (2009).

[4] S. A. Diddams, K. Vahala, and T. Udem, Optical frequency combs: Coherently uniting the electromagnetic spectrum, *Science* **369**, 267 (2020).

[5] T. Laarmann, I. Shchatsin, R. Wu, A. Pechen, D. I. Bondar, and A. N. Pechen, Control of quantum phenomena: past, present and future, *New Journal of Physics* **12**, 075008 (2010).

[6] J. Mizrahi, C. Senko, B. Neyenhuis, K. G. Johnson, W. C. Campbell, C. W. S. Conover, and C. Monroe, Ultrafast Spin-Motion Entanglement and Interferometry with a Single Atom, *Physical Review Letters* **110**, 203001 (2013), arXiv:arXiv:1201.6597v2.

[7] C. P. Koch, Quantum control of molecular rotation, *Reviews of Modern Physics* **91**, 35005 (2019).

[8] M. Maiuri, M. Garavelli, G. Cerullo, M. Maiuri, M. Garavelli, and G. Cerullo, Ultrafast spectroscopy : state of the art and open challenges, *Journal of the American Chemical Society* **9**, 10533 (2019).

[9] N. Picqué and T. W. Hänsch, Frequency comb spectroscopy, *Nature Photonics* **13**, 10.1038/s41566-018-0347-5 (2019).

[10] A. M. Weiner, Femtosecond pulse shaping using spatial light modulators, *Review of Scientific Instruments* **71**, 1929 (2000).

[11] A. Monmayrant, A newcomer 's guide to ultrashort pulse shaping and characterization, *J. Phys. B: At. Mol. Opt. Phys* **43**, 103001 (2010).

[12] S.-w. Chiow, S. Herrmann, and S. Chu, Nanosecond electro-optical switching with a repetition rate above 20 MHz., *Rev. Sci. Instrum.* **78**, 124702 (2007), arXiv:arXiv:0710.1374v2.

[13] E. A. Donley, T. P. Heavner, F. Levi, M. O. Tataw, and S. R. Jefferts, Double-pass acousto-optic modulator system, *Rev. Sci. Instrum.* **76**, 063112 (2005).

[14] J. Thom, G. Wilpers, E. Riis, and A. G. Sinclair, Accurate and agile digital control of optical phase , amplitude and frequency for coherent atomic manipulation of atomic systems, *Opt. Express* **21**, 18712 (2013).

[15] C. Zhou, C. He, S. T. Yan, Y. H. Ji, L. Zhou, J. Wang, and M. S. Zhan, Laser frequency shift up to 5 GHz with a high-efficiency 12-pass 350-MHz acousto-optic modula-
tor, *Rev. Sci. Instrum.* **91**, 033201 (2020).

[16] T. S. Khwaja and T. H. Yoon, Phase-stable and selectable repetition-rate division of an optical frequency comb, *Phys. Rev. A* **102**, 043515 (2020).

[17] S. Koke, C. Grebing, H. Frei, A. Anderson, A. Assion, and G. Steinmeyer, Direct frequency comb synthesis with arbitrary offset and shot-noise-limited phase noise, *Nat. Photonics* **4**, 462 (2010).

[18] Z. Chen, M. Yan, T. W. Hänsch, and N. Picqué, A phase-stable dual-comb interferometer, *Nat. Commun.* **9**, 3035 (2018), arXiv:1705.04214.

[19] J. Hirschman, R. Lemons, E. Chansky, G. Steinmeyer, and S. Carbo, Long-term hybrid stabilization of the carrier-envelope phase, *Opt. Express* **28**, 34093 (2020), arXiv:2006.02647.

[20] Y.-J. Wang, D. Anderson, V. Bright, E. Cornell, Q. Diot, T. Kishimoto, M. Prentiss, R. Saravanan, S. Segal, and S. Wu, Atom michelson interferometer on a chip using a Bose-Einstein condensate, *Physical Review Letters* **94**, 090405 (2005).

[21] S. Wu, Y.-J. Wang, Q. Diot, and M. Prentiss, Splitting matter waves using an optimized standing-wave light-pulse sequence, *Phys. Rev. A* **71**, 043602 (2005).

[22] K. J. Hughes, B. Deissler, J. H. T. Burke, and C. A. Sackett, High-fidelity manipulation of a Bose-Einstein condensate using an optical standing wave, *Physical Review A* **76**, 035601 (2007).

[23] G. T. Genov and N. V. Vitanov, Dynamical Suppression of Unwanted Transitions in Multistate Quantum Systems, *Phys. Rev. Lett.* **110**, 133002 (2013).

[24] G. T. Genov, D. Schraft, T. Halfmann, and N. V. Vitanov, Correction of Arbitrary Field Errors in Population Inversion of Quantum Systems by Universal Composite Pulses, *Phys. Rev. Lett.* **113**, 043001 (2014).

[25] G. H. Low, T. J. Yoder, and I. L. Chuang, Methodology of resonant equiangular composite quantum gates, *Phys. Rev. X* **6**, 041067 (2016), arXiv:1603.03996.

[26] M. Endres, H. Bernien, A. Keesling, H. Levine, E. R. Anschuetz, A. Krajenbrink, C. Senko, V. Vuletic, M. Greiner, and M. D. Lukin, Atom-by-atom assembly of defect-free one-dimensional cold atom arrays, *Science* **354**, 1024 (2016).

[27] H. Tunnermann and A. Shirakawa, Delay line coherent pulse stacking of a symmetric mode-locked pulse train, *Opt. Lett.* **42**, 4829 (2017).

[28] A. Klenke, M. Muller, H. Stark, M. Kienel, C. Jauregui, A. Tunnermann, and J. Limpert, Coherent Beam Combination of Ultrafast Fiber Lasers, *IEEE J. Sel. Top. Quant.*

tum Electron. **24**, 0902709 (2018).

[29] G. T. Genov, A. A. Rangelov, and N. V. Vitanov, Efficient broadband frequency generation in composite crystals, *J. Opt.* **16**, 062001 (2014).

[30] A. B. M. Essaadi, M. A. M. S. Á. Ópez, P. A. G. A. Artínez, and I. G. M. Oreno, Achromatic linear retarder with tunable retardance, *Opt. Lett.* **43**, 3277 (2018).

[31] J. F. F. Bulmer, J. A. Jones, and I. A. Walmsley, Drive-noise tolerant optical switching inspired by composite pulses, *Opt. Express* **28**, 8646 (2020).

[32] Y. He, L. Ji, Y. Wang, L. Qiu, J. Zhao, Y. Ma, X. Huang, S. Wu, and D. E. Chang, Geometric control of collective spontaneous emission, *Physical Review Letters* **125**, 213602 (2020), arXiv:1910.02289.

[33] C. E. Rogers III and P. L. Gould, Nanosecond Pulse Shaping with Fiber-Based Electro-Optical Modulators and a Double-Pass Tapered Amplifier, *Optics Express* **24**, 2596 (2015), arXiv:arXiv:1511.01228v1.

[34] Y. Vidne, M. Rosenbluh, and T. W. Hansch, Pulse picking by phase-coherent additive pulse generation in an external cavity, *Optics Letters* **28**, 2396 (2003).

[35] P. Tournois, Compensation of group delay time dispersion in laser systems, *Opt. Commun.* **4018**, 245 (1997).

[36] S. Zhang, Z. Fu, B. Zhu, G. Fan, Y. Chen, S. Wang, Y. Liu, A. Baltuska, C. Jin, C. Tian, and Z. Tao, Solitary beam propagation in periodic layered Kerr media enables high-efficiency pulse compression and mode self-cleaning, *Light: Science and Applications* **10**, 53 (2021).

[37] D. Zhang, M. N. Slipchenko, D. E. Leaird, A. M. Weiner, and J.-X. Cheng, Spectrally modulated stimulated Raman scattering imaging with an angle-to-wavelength pulse shaper, *Optics Express* **21**, 13864 (2013).

[38] M. Andreana, M.-A. Houle, D. J. Moffatt, A. Ridsdale, E. Buettner, F. Légaré, and A. Stolow, Amplitude and polarization modulated hyperspectral Stimulated Raman Scattering Microscopy, *Optics Express* **23**, 28119 (2015).

[39] R. He, L. Zhang, X. Miao, and M. Ji, Dual-phase stimulated Raman scattering microscopy for rapid, label-free histology, *Optica* **4**, 44 (2017).